

# Motion-based Object Segmentation based on Dense RGB-D Scene Flow

Lin Shao, Parth Shah\*, Vikranth Dwaracherla\*, and Jeannette Bohg

**Abstract**—Given two consecutive RGB-D images, we propose a model that estimates a dense 3D motion field, also known as *scene flow*. We take advantage of the fact that in robot manipulation scenarios, scenes often consist of a set of rigidly moving objects. Our model jointly estimates (i) the segmentation of the scene into an unknown but finite number of objects, (ii) the motion trajectories of these objects and (iii) the object scene flow. We employ an hourglass, deep neural network architecture. In the encoding stage, the RGB and depth images undergo spatial compression and correlation. In the decoding stage, the model outputs three images containing a per-pixel estimate of the corresponding object center as well as object translation and rotation. This forms the basis for inferring the object segmentation and final object scene flow. To evaluate our model, we generated a new and challenging, large-scale, synthetic dataset that is specifically targeted at robotic manipulation: It contains a large number of scenes with a very diverse set of simultaneously moving 3D objects and is recorded with a simulated, static RGB-D camera. In quantitative experiments, we show that we outperform state-of-the-art scene flow and motion-segmentation methods on this data set. In qualitative experiments, we show how our learned model transfers to challenging real-world scenes, visually generating better results than existing methods.

## I. INTRODUCTION

Semantic and functional scene understanding is a crucial capability of manipulation robots. In the Computer Vision community, this challenging problem is often approached given only a single image. However, a robot is able to physically interact with the environment and thereby autonomously induce motion in the scene. This motion creates a rich, visual sensory signal that would otherwise not be present, thus facilitating better scene understanding. Methods that exploit physical interaction to ease perception are often referred to as performing *Interactive Perception* (IP) [1]. In this paper, we are providing the robot with a model to process the visual effect of its interaction. Given two consecutive RGB-D images, we are interested in estimating a dense 3D motion field of the environment, also known as *scene flow*. We show how this result helps to segment the finite, but unknown number of moving objects in the scene. This can provide input to tasks such as for example grasp planning or 3D object reconstruction.

We propose a model that takes advantage of the fact that in a common household scenario, scenes often consist of a set of rigidly moving objects. Our model jointly estimates (i) the segmentation of a scene into a finite number of rigidly moving object, (ii) the motion trajectories of these objects and (iii) the resulting *object scene flow* [26]. We propose to use a deep neural network architecture that takes as input a pair of consecutive RGB-D images. See Fig. 1 for an overview of the approach. In a first stage, features

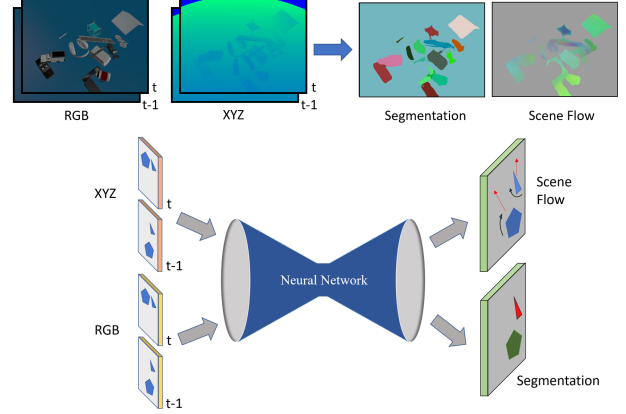


Fig. 1. We present a neural network which learns to estimate object segmentation and scene flow given a pair of RGB-D images. The data undergoes spatial compression, correlation, and refinement to propose object segmentations and transformations.

are extracted from each of the four input images. The RGB features are then correlated and the resulting values are used to weight the feature encoding of the depth data. Intuitively, this favors correspondences between points in the depth data that also have a strong similarity in the RGB images. The result is then decoded to produce three images containing the object positions, their translation, and their rotation. From this, we can infer the object scene flow and segmentation.

Our primary contributions are: (1) generating a challenging, large-scale dataset for scene flow estimation with ground-truth annotated RGB-D images, (2) treating rotational symmetry of objects in scene flow prediction, (3) estimating object scene flow with a deep neural network architecture, and (4) predicting rigid body transformations to segment a finite, but unknown number of moving objects.

## II. RELATED WORK

Estimating scene flow has a long-standing history in the research community starting with Vedula et al. [33]. We briefly review the most recent approaches that are related to our work in terms of several aspects: input sensor, data sets, learning-based methods and motion segmentation.

### A. Scene Flow based on RGB-D or Stereo Images

Gottfried et al. [12] were the first to use an RGB-D sensor for scene flow estimation. Their work also addresses the necessary calibration process. Herbst et al. [17] generalize the two-frame variational optical flow algorithm (2D) to scene flow (3D). The resulting dense scene flow is then used for rigid motion segmentation. Jaimez et al. [19] present the first real-time method for computing dense scene flow from RGB-D images. Their method is based on a variational formulation that imposes brightness and geometric consistencies. The minimization problem is efficiently solved with a GPU and a primal-dual algorithm. Vogel et al.

\*The authors contributed equally.

The authors are with Stanford University, CA, USA. [lins2, pshah9, vikranth, bohg]@stanford.edu

[34] were the first to propose the estimation of piecewise rigid scene flow where oversegmentation into superpixels constrains the scene flow estimation. The authors obtain a new level of accuracy that may run in real-time. Inspired by this work, Golyanik et al. [11] propose a multi-frame scene flow approach which jointly optimizes the consistency of the patch appearances and their local motions from RGB-D image sequences. However the reliance on bottom up cues for segmentation may lead to oversegmentation of objects. Menze and Geiger [26] defined *object scene flow* as the 3D motion associated with a set of pixels that constitute a rigidly-moving object. By assuming that the scene consists of a set of such objects and encouraging superpixels in the same region to have similar 3D motion, the authors constrain the solution space for estimating scene flow. The inference process is computationally very expensive, taking 2-50 minutes per image pair.

For computing a matching score between pixels across stereo frames and over time, traditional approaches often rely on assumptions like brightness constancy and motion smoothness within a small region. In real scenes, these assumptions are often broken for example with non-Lambertian surfaces, occlusions or large displacements. These effects are prevalent when multiple objects are moving fast and simultaneously over time. Therefore, matching pixel positions over time is the most vulnerable component in traditional methods. Our hypothesis is that these challenges can be mitigated by using methods that learn powerful features of the raw input data over multiple spatial scales. Evidence comes from successful learning-based approaches towards optical flow as detailed in Sec. II-C.

## B. Datasets

Several large scale datasets exist for benchmarking and learning optical and scene flow. Different from our data set, they are all under a binocular setting with flow and disparity ground truth. KITTI [10] consists of 194 training and 195 test scenes recorded from a calibrated pair of cameras mounted on a car. Ground truth annotations are obtained by combining data from a 3D laser scanner with the car’s ego motion. Menze and Geiger [26] annotated the dynamic scenes with 3D CAD models for all moving vehicles and modified the dataset with 200 training scenes and 200 test scenes. KITTI contains valuable real world data. However, the ground truth contains some approximation error. Mayer et al. [25] created a synthetic dataset called FlyingThings3D containing over 35000 stereo frames with ground truth scene flow annotations. When using data from stereo cameras, insufficient texture can result in matching errors across frames and over time. RGB-D cameras deliver dense depth measurements despite a lack of texture. This data can support the matching process. Therefore, our data set contains pairs of consecutive RGB-D images and is of similar size as FlyingThings3D. Different from the aforementioned datasets, objects in our dataset are falling onto a surface, colliding with each others, and even sliding on the surface. It is important for a manipulation robot to understand this type of non-smooth, physically-realistic motion due to contact. The objects in our scenes are also much closer to each

other, leading to more challenging occlusions and motion. And lastly, we use a new annotation method to coherently label objects with rotational symmetry. See Section V for more details on our dataset.

## C. Learning-Based Flow Prediction

Learning-based methods have up till now been mainly applied to optical flow estimation. Dosovitskiy et al. [8] posed this problem as a supervised learning problem and were the first to solve it with *Convolutional Neural Networks* (CNNs). They compare two architectures called FlowNetS and FlowNetC: a generic architecture and an architecture that includes a layer that correlates feature vectors at different image locations. These two FlowNets were tested on datasets like Sintel [4] and KITTI [10] achieving competitive accuracy at frame rates of 5-10 fps. Ilg et al. [18] extend FlowNet by developing a stacked architecture. It includes warping of the second images with intermediate optical flow. The authors also propose a subnetwork specializing in small displacements resulting in state-of-the-art results while running at real-time. For learning-based scene flow estimation, Hadfield and Bowden [15] introduced a novel cost function. In this new formulation, only a limited portion of the parameters from the entire pipeline are learned, leading to limited improvements. Mayer et al. [25] utilized a CNN to estimate scene flow based on stereo images. They embed a disparity estimation network called DispNet into FlowNet [8]. We propose an hourglass deep architecture that uses two RGB-D frames as input. It adopts the correlation layer of FlowNetC for the RGB encoding and uses this to associate encoded point cloud features. One of our main contributions is the decoder which directly predicts object position, translation and rotation. From this we can infer object scene flow and motion-based, rigid object segmentation.

## D. Motion-based Segmentation

Bohg et al. [1] extensively review the variety of work towards motion-based segmentation within robotics. Here, we discuss a few representative examples. Many works use over-segmentations and connect superpixels over time using clustering methods [2, 13]. However, the reliance on bottom-up cues often results in some remaining oversegmentation. The authors of [6, 3, 37] formulate the problem as clustering of point trajectories across different frames and solve it based on spectral clustering methods. Instead, Rahmati et al. [29] utilize multi-label graph cuts. Ji et al. [21] define an unbalanced energy to model both, motion segmentation and point matching. Keuper et al. [23] formulate motion-based segmentation based on point trajectories as a minimum cost, multi-cut problem. The minimum cost multi-cut formulation allows for varying cluster sizes. We propose a model where each pixel directly predicts the center and trajectory of the object that it is associated with. We achieve accurate motion-based segmentation by clustering in this space. This in turn helps to refine the scene flow estimate.

## III. PROBLEM FORMULATION & NOTATION

The input to the proposed model are two consecutive RGB-D images. We assume that the environment consists

of a finite, but unknown, number of rigidly moving objects. The network outputs (i) a pixel-wise segmentation of each object, (ii) the rigid body motion of each object, and (iii) the scene flow of each pixel in a reference frame.

More formally, let  $\mathcal{I}^t$  and  $\mathcal{P}^t$  denote an RGB image and a point cloud from a single RGB-D image at time  $t$ . Time  $t$  and  $t - 1$  refer to the current and previous frames, respectively. To calculate scene flow of each point  $P_i^t \in \mathcal{P}^t$  in a reference frame, we predict its 3D displacement by estimating its corresponding position  $P_i^{t-1}$  in the previous frame. This estimate is denoted by  $\hat{P}_i^{t-1}$ .

Let  $\mathcal{O}$  denote the set of rigidly moving objects in the scene. The rigid body motion between two consecutive frames for  $\mathcal{O}_k$  is described by an SE(3) transform consisting of a rotation  $R_k$  and translation  $T_k$ . Our model directly outputs three images  $\mathcal{Q}$ ,  $\mathcal{T}$  and  $\mathcal{X}$  where each pixel contains an estimate of the rotation, translation and center of the object that the pixel belongs to. Therefore, if point  $P_i^t$  is generated by  $\mathcal{O}_k$  then the correct value at the projected image coordinates  $(u, v)$  in the respective output images will contain the ground truth rotation, translation and center of object  $\mathcal{O}_k$ .

We denote the rotation of a point  $P_i$  based on the axis-angle representation  $Q_k$  as  $r(P_i, Q_k) = R_k P_i$ . Therefore, the corresponding point in frame  $t - 1$  can be computed by

$$P_i^{t-1} = r(P_i^t - X_k, Q_k) + X_k + T_k \quad (1)$$

with per-pixel scene flow  $S_i = P_i^{t-1} - P_i^t$ . Note, that our model outputs an estimate of the ground truth variables  $Q_k, T_k$  and  $X_k$  which results in  $\hat{P}_i^{t-1}$  instead of  $P_i^{t-1}$  and therefore only in an estimate  $\hat{S}_i$  of the ground truth scene flow. During training, we aim to minimize the error between these estimates and the ground truth.

Let  $\xi_k = [X_k, X_k + T_k]$  be the trajectory feature of an object  $\mathcal{O}_k$ .  $X_k$  and  $X_k + T_k$  are the object centers at frame  $t$  and  $t - 1$ , respectively. Unless two objects have exactly the same object center and move with exactly the same translation trajectory, each  $\xi_k$  is unique per object. Therefore, we can use it as a cue for motion-based, object segmentation.

#### IV. TECHNICAL APPROACH

##### A. Rigid Motion and Object Scene Flow

The first stage of the proposed model, displayed in Fig. 2, consists of two Siamese networks that takes RGB images  $\mathcal{I}^{t-1}$ ,  $\mathcal{I}^t$  and point clouds  $\mathcal{P}^{t-1}$ ,  $\mathcal{P}^t$  as inputs, each with resolution  $(W, H, 3)$ . The pair of point clouds is fed into the first of these networks that outputs a new feature encoding denoted by  $\mathcal{P}^{f^{t-1}}$  and  $\mathcal{P}^{f^t}$ , respectively. We use the VGG architecture [32] for this purpose. The shape of the output feature is  $(W/8, H/8, 64)$ .

The pair of RGB images is fed into the second Siamese network that outputs a new feature encoding denoted by  $\mathcal{I}^{f^{t-1}}$  and  $\mathcal{I}^{f^t}$ , respectively. We use the ResNet50 architecture and its weights for initialization [16]. The shape of the output feature tensor is  $(W/8, H/8, 256)$ .

The RGB image features are fed into a correlation layer similar to the one used in FlowNetC [8]. A high correlation between patches in consecutive RGB images indicates that they contain a projection of the same physical object part.

This correlation layer parallels the brightness constancy assumption in traditional optical and scene flow methods.

Fig. 3 visualizes the correlation process encoded in the layer. Let  $\mathcal{I}_{uv}^{f^t}$  denote a feature of RGB image  $\mathcal{I}^t$  at pixel  $(u, v)$ . Each feature is correlated with a patch of features denoted by  $\mathcal{P}\mathcal{I}_{uv}^{f^{t-1}}$ . The patch is centered at  $\mathcal{I}_{uv}^{f^{t-1}}$  and has a side length of  $2L + 1$ , i.e. the dimension of the patch encoding is  $(2L + 1, 2L + 1, 256)$ . The correlation operation between features  $\mathcal{I}_{uv}^{f^t}$  and  $\mathcal{I}_{kl}^{f^{t-1}}$  inside the patch  $\mathcal{P}\mathcal{I}_{uv}^{f^{t-1}}$  is defined as

$$c(\mathcal{I}_{uv}^{f^t}, \mathcal{I}_{kl}^{f^{t-1}}) = \langle \mathcal{I}_{uv}^{f^t}, \mathcal{I}_{kl}^{f^{t-1}} \rangle \text{ if } |u - k| \leq L, |v - l| \leq L \quad (2)$$

The output vector of correlation between the single feature  $\mathcal{I}_{uv}^{f^t}$  and corresponding patch  $\mathcal{P}\mathcal{I}_{uv}^{f^{t-1}}$  has a dimension of  $(2L + 1)^2$ . The correlation is performed at each pixel within  $\mathcal{I}^{f^{t-1}}$  with a stride of  $(W/8, H/8)$ . The final output shape of the correlation layer is  $(W/8, H/8, (2L + 1)^2)$ .

Highly correlated RGB patches also indicate which parts in consecutive point clouds correspond to each other. We therefore multiply the correlation value tensor with the corresponding  $\mathcal{P}^{f^{t-1}}$  features to get a weighted XYZ feature encoding  $\widehat{\mathcal{P}}^{f^{t-1}}$ . Then we apply max pooling to this result along the feature dimension as follows:

$$\widehat{\mathcal{P}}_{uv}^{f^{t-1}} = \max_{\substack{|u-k| \leq L \\ |v-l| \leq L}} (c(\mathcal{I}_{uv}^{f^t}, \mathcal{I}_{kl}^{f^{t-1}}) \mathcal{P}_{kl}^{f^{t-1}}) \quad (3)$$

We concatenate  $[\mathcal{P}^{f^t}, \mathcal{P}^{f^{t-1}}, \widehat{\mathcal{P}}^{f^{t-1}}]$  and feed this into another encoder until reaching a feature map with size  $(W/60, H/60, 512)$  before feeding it into a decoder. Skip links are created between encoder and decoder. The decoder generates three images  $\mathcal{Q}$ ,  $\mathcal{T}$  and  $\mathcal{X}$  representing per-pixel estimates of rotation, translation and center position of the object projected to that pixel. Per-pixel scene flow can then be computed through Eq. 1.

##### B. Motion-based Segmentation

As defined previously, let  $\xi_k = [X_k, X_k + T_k]$  represent the start and end point of the object trajectory of  $\mathcal{O}_k$ . Pixels belonging to the same object  $\mathcal{O}_k$  will have the same value  $\xi_k$ . We assume that pixels belonging to different objects have different values. Based on this we perform object segmentation.

Our model makes a pixel-wise prediction  $\hat{\xi}_{uv}$  of the trajectory feature at pixel coordinates  $(u, v)$ . This is only an approximation of the ground truth value. Therefore, each pixel  $(u, v)$  that corresponds to the same object  $\mathcal{O}_k$  will predict feature values  $\hat{\xi}_{uv}$  that differ from ground truth by some  $\epsilon_{uv}$  such that  $\hat{\xi}_{uv} = \xi_{uv} + \epsilon_{uv}$ .

To segment moving objects, we propose the following inference process. Let  $\mathcal{B}$  be an additional output image of our model. A pixel at  $(u, v)$  contains a scalar value  $B_{uv}$ . This value is a radius estimate of the sphere that encloses all pixels which belong to the same moving object, i.e. have a similar trajectory. The sphere is centered at  $\hat{\xi}_{uv}$ . Any pixel at coordinates  $(o, p)$  whose  $\hat{\xi}_{op}$  falls inside the sphere centered around  $\hat{\xi}_{uv}$  will be segmented as the same object  $\mathcal{O}_k$ . Any pixel at  $(m, n)$  whose  $\hat{\xi}_{mn}$  falls outside the sphere will be

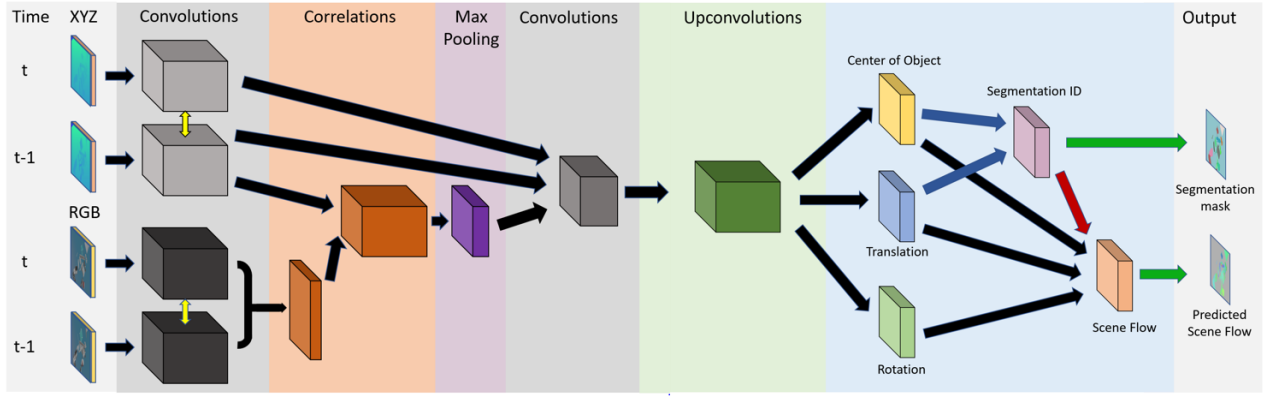


Fig. 2. Network architecture utilized in this paper. The RGB-D input is split into two components, RGB and XYZ, before being passed into Siamese neural networks. A correlation is performed on the output of the RGB Siamese network and applied to the XYZ features from time  $t - 1$ . After a max pooling layer, the newly combined features undergo upconvolutions. The output of the upconvolutions is fed into 3 different layers that predict the center of the object, translation, and rotation. Thereafter, the segmentation ID is determined using the center of the object and its predicted translation. For predicting scene flow, the translation, rotation, and input XYZ data is utilized. The final output is presented as a segmentation mask and scene flow predictions. Note that the blue, red, and green arrows do not have gradient flow.

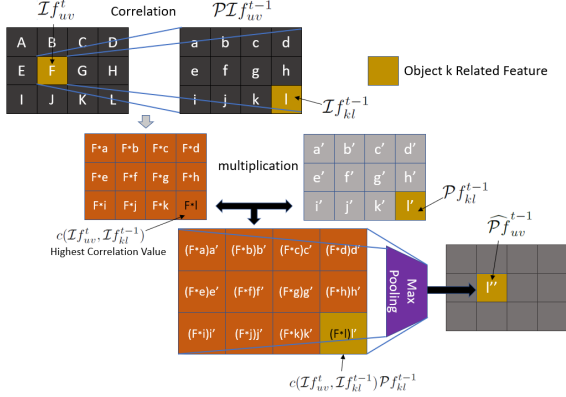


Fig. 3. Process of correlation and max-pooling. After two RGB feature maps (black) are generated, each cell in the feature map  $\mathcal{I}_f^t$  is correlated with every cell within a patch of the feature map  $\mathcal{I}_f^{t-1}$ . Let us assume that the yellow cells  $F$  and  $I$  contain features corresponding to the same object. Therefore, their correlation  $c(\mathcal{I}_f^t, \mathcal{I}_f^{t-1})$  will be high. These correlation values are used to weight corresponding cells of the XYZ feature map  $\mathcal{P}_f^{t-1}$  (gray). The result is fed into a max-pooling layer which in this example will output  $c(\mathcal{I}_f^t, \mathcal{I}_f^{t-1})\mathcal{P}_f^{t-1}$ . The final feature  $I''$  containing object XYZ information at frame  $t - 1$  will be placed at the same location as feature  $F$  at frame  $t$ .

part of the background or a different object. In addition to  $\mathcal{B}$ , we also learn a mask layer to discard pixel in this segmentation process that belong to the background.

To generate the ground truth of  $\mathcal{B}^{gt}$ , each pixel  $(u, v)$  representing object  $\mathcal{O}_k$  is annotated by half of the minimum distance between  $\xi_k$  and the trajectories  $\xi_l$  of all the other objects in the image pair:

$$\mathcal{B}_{uv}^{gt} = \frac{1}{2} \min_{k \neq l} \|\xi_k - \xi_l\|_2 \quad (4)$$

Inspired by region proposals [30], our model also outputs an image denoted by  $\eta$ . Each pixel in this image at  $(u, v)$  contains the probability  $\eta_{uv}$  that it is the projection of the object centroid. To generate the ground truth of  $\eta$ , we sort pixels representing object  $\mathcal{O}_k$  by their distance to the object's centroid in ascending order. The top  $D$  pixels per object in the input image  $\mathcal{I}$  will be labeled as 1, the rest will be labeled as 0. If the total number of pixels representing object  $\mathcal{O}_k$  is less than  $D$ , all of them are labeled as 1. We found that  $D =$

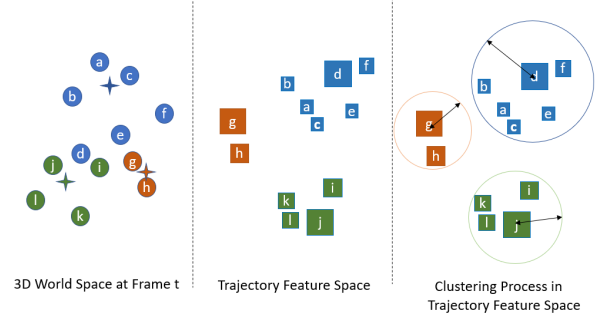


Fig. 4. Object segmentation process. Left: Points represent points in a point cloud. Stars represent ground-truth object centers. Same color indicates same object. Middle: Each square represents the trajectory features  $\hat{\xi}$  in trajectory feature space each associated with a point on the left. The size of the squares represents the corresponding point's probability  $\hat{\eta}$  of being an object centroid. Right: The segmentation process cycles through the squares starting with those having the highest probability to be an object centroid. A sphere centered at one of those squares with radius  $\hat{\mathcal{B}}$  then segments trajectories and corresponding points.

300 worked well. This corresponds to approximately 10% - 30% of the ground truth object pixels. The final performance is not very sensitive to this parameter

Given the predicted  $\hat{\mathcal{B}}$  and  $\hat{\eta}$ , we can now perform multi-object segmentation as visualized in Fig. 4. Pixel  $(u, v)$  with the maximum predicted probability  $\hat{\eta}_{uv}$  is proposed first. Given a sphere centered at  $\hat{\xi}_{uv}$  with radius  $\hat{\mathcal{B}}_{uv}$ , all pixels  $(m, n)$  with a trajectory  $\hat{\xi}_{mn}$  enclosed by this sphere are assigned to object  $\mathcal{O}_1$ . All pixel assigned to  $\mathcal{O}_1$  are removed from the set of unsegmented pixels before segmenting the next object. The remaining pixel at  $(o, p)$  with the highest  $\hat{\eta}_{op}$  is used as the seed for segmenting  $\mathcal{O}_2$ . This process is repeated until all foreground pixels are assigned an object id  $k$ . The final object translation  $T_k$  and rotation  $R_k$  is computed by averaging over all pixels with the same id. Based on this, also the scene flow can be recomputed.

### C. Loss Function

We use the following training loss:

$$L = \lambda_m L_m + \lambda_{center} L_{center} + L_p + \lambda_{var} L_{var} + \lambda_{vio} L_{vio}. \quad (5)$$

In the following, we define each term. Note that all pixel-wise loss terms  $L_p$ ,  $L_{center}$ ,  $L_{var}$  and  $L_{vio}$  are only computed on the ground truth foreground pixel.

1) *Mask Loss*:  $L_m$  is the cross entropy loss between the ground truth and estimated foreground/background segmentation. If a pixel is the projection of an object point, we assign 1 as ground truth; otherwise 0.

2) *Cluster Center Loss*: Cross-entropy loss  $L_{center}$  is used to learn the probability  $\eta_{uv}$  of a pixel  $(u, v)$  to be the object center as described in Sec. IV-B.

3) *Pixel-wise Loss*: We use a pixel-wise loss  $L_p$  on the predicted object rotation  $Q_{uv}$ , translation  $T_{uv}$ , scene flow  $S_{uv}$ , enclosing sphere radius  $B_{uv}$  and trajectory  $\xi = [X_{uv}, X_{uv} + T_{uv}]$ . For each attribute, we use the L2-norm to measure and minimize the error between predictions and ground truth. Note that the loss on each attribute is also differently weighted. We denote their corresponding weights  $\lambda_Q$ ,  $\lambda_T$ ,  $\lambda_X$ ,  $\lambda_S$ ,  $\lambda_B$  and  $\lambda_\xi$ .

4) *Variance Loss*: We use  $L_{var}$  to encourage pixels  $(u, v)$  belonging to the same object  $\mathcal{O}_k$  to have similar trajectories  $\xi_{uv}$  and thereby to reduce their variance.

$$L_{var} = \sum_k \frac{1}{N_k} \sum_{(u,v) \in \mathcal{O}_k} \|\hat{\xi}_{uv} - \bar{\xi}_{uv}\|^2 \quad (6)$$

where  $\bar{\xi}_{uv}$  is the mean value of  $\hat{\xi}_{uv}$  over all  $N_k$  pixels belonging to  $\mathcal{O}_k$ .

5) *Violation Loss*:  $L_{vio}$  penalizes pixels  $(u, v)$  that are not correctly segmented. Any predicted trajectory  $\hat{\xi}_{uv}$  that is more than  $\frac{1}{5}B_{uv}$  away from the ground truth  $\xi_{uv}$  will be pushed towards the ground truth trajectory by the violation loss. Note that  $B_{uv}$  refers to the radius of enclosing sphere.

$$L_{vio} = \sum_k \sum_{(u,v) \in \mathcal{O}_k} \mathbf{1}\{\|\hat{\xi}_{uv} - \xi_{uv}\|_2 > \frac{1}{5}B_{uv}\} \|\hat{\xi}_{uv} - \xi_{uv}\|_2$$

The variance and violation loss are designed to train the clustering framework described in IV-B.

## V. DATASET

We generated a new dataset that consists of RGB-D image pairs showing dynamic scenes. These scenes contain a large variety of rigidly-moving objects. See Fig. 9 for some example frames. To ensure a diverse data set, we used 31594 3D object mesh models from ShapeNet [5] covering 28 categories. We split these models into a training, validation and test set with 21899, 3186 and 6509 objects respectively. Model sizes are adjusted to simulate their real world sizes [31]. For each scene, 1-30 object models are randomly selected. For simulating realistic object motion, we use Bullet [7] as physics engine. The objects are put close to each other at 0.2 meter above a surface. After simulation begins, they start to fall down to the surface and collide with each other in the process. The RGB-D camera is static and the simulation runs at 60 Hz. We extract frame 20 and 80 from the simulated image sequence as RGB-D image pair. They are 1 second apart with an average object displacement of 0.085 meters. We synthesize 24994, 3360 and 7186 frame pairs for training, validation and test set. Note that the object

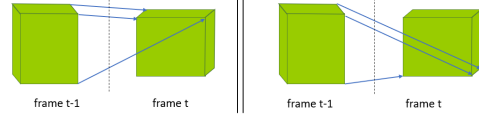


Fig. 5. A rotationally symmetric object for which two different rotations yield the same RGB-D data. Therefore, multiple solutions for scene flow exist.

models are not re-used across these data sets. In total, we generated 35540 pairs of consecutive RGB-D frames using Blensor [14] to ensure realistic depth data. For each rendered RGB image pair, we randomly sample an image from the SUN397 dataset [35] to simulate textured floor or we use a single color. We also randomly change the lighting conditions (number of light sources, their positions and energies) and camera viewpoint. We do not add artificial noise in the raw dataset for two reasons. Different sensors like time-of-flight or structured light have different noise patterns. Adding one type of noise pattern into the dataset might increase the simulation-to-reality gap when other sensors are used. Extra noise can be dynamically added into the neural network training procedure as data augmentation procedure.

### Annotating Objects with Rotational Symmetry

Some of the objects in ShapeNet [5] are rotationally symmetric, e.g. bottles and bowls. Rotational symmetry is a common object attribute especially for human-made objects. However, the rotation of such an object around its symmetry axis is not observable in an image pair (especially when uniformly colored) as there might be multiple or even infinite solutions. There are different orders of rotational symmetry denoted by  $C_2, \dots, C_n, \dots, C_\infty$ . An object with  $C_n$  means that it will remain the same after rotating about the rotation axis by  $\pm 360/n$  degrees. An object might contain several different rotational symmetries. Fig. 5 illustrates an example.

This has implications for the ground truth annotation of our dataset. If we directly use the ground truth rotation provided by the simulator, the network might not converge during training as more than one rotation might lead to the same RGB-D data. In the following, we describe a procedure to map the ground truth rotation of an object about its symmetry axis to the rotation with minimum angular displacement. Consider an object with  $C_n$  rotational symmetry. Let  $\bar{r}_{t-1}$  and  $\bar{r}_t$  denote this axis of symmetry at frame  $t-1$  and frame  $t$ , respectively. Let the rotation provided by the simulator be given as a quaternion  $q = [q_0, q_x, q_y, q_z]^T$ . We decompose the rotation  $q$  into a rotation  $\alpha$  about  $C_n(\bar{r}_{t-1})$  and a rotation  $\theta$  perpendicular to  $C_n$ : ( $\bar{r}_\perp = \bar{r}_{t-1} \times \bar{r}_t$ ).

$$\alpha = 2 \tan^{-1} \left( \frac{r_{t-1,x}q_x + r_{t-1,z}q_z + r_{t-1,y}q_y}{q_0} \right) \quad (7)$$

$$\theta = 2 \cos^{-1} (q_0 / \cos(\frac{\alpha}{2})) \quad (8)$$

$\alpha$  is then adjusted to be  $\hat{\alpha} \in (-\pi/n, \pi/n]$ . This corresponds to the minimum angular displacement leading to the same observation as the original angle. From this, we can construct a new quaternion  $\hat{q}$  which corresponds to the rotation of  $\hat{\alpha}$  about  $\bar{r}_{t-1}$  and rotation of  $\theta$  about  $\bar{r}_\perp$ . Note that if  $\alpha = \hat{\alpha} \in (-\pi/n, \pi/n]$  then  $q = \hat{q}$ . This operation is performed on all the rotational axis of symmetry. With this procedure,



we reduced the ambiguous cases to a very small number, e.g. to uniformly-colored objects with non-orthogonal axes of symmetry (of which there exists one among our models) or rotations as shown in Fig. 5 where the minimum angular displacement can either refer to a rotation in the positive or negative direction.

## VI. EXPERIMENTS

We report the performance of the proposed model quantitatively on the synthesized dataset and qualitatively on real data. We evaluate accuracy in scene flow prediction by comparing to PD-Flow [19], semi-rigid scene flow (SR-Flow) [28] and Jaimez et al. [20]. We evaluate motion-based segmentation performance by comparing to Higher-Order Minimum Cost Lifted Multicuts (HOMC) [22].

Furthermore, we compare to variants of the proposed architecture. We refer to the network in Fig. 2 as **OurC** and propose a simpler neural net architecture denoted by **OurS**. It concatenates all four input images and feeds it into the encoder. Most importantly, it drops the correlation and max pooling layer. The remaining model architecture is the same. **OurC+vL** denotes added variance and violation loss compared to training **OurC**. Our model **OurC+vL** simultaneously predicts pixel-level segmentation IDs and scene flow. Given all pixels with the same, predicted object ID, we compute the mean object center  $\bar{X}_k$ , translation  $\bar{T}_k$  and rotation  $\bar{Q}_k$ . **OurC+vL+Rig** denotes the model with added rigidity constraints for improved scene flow estimation. After we infer the segmentation mask per object, we average the rigid transformations from pixels predicted to represent the same object. The rigid transformation is then applied to pixels to recalculate scene flow.

We conduct our experiments on an NVIDIA P100 with TensorFlow. For training, we use the Adam optimizer [24] with its suggested default parameters of  $\beta_1 = 0.9$  and  $\beta_2 = 0.999$  along with a learning rate  $\alpha = 0.0001$  [24]. We use a batch size of 12 image pairs. The input RGB-D images have a resolution of  $240 \times 320$ . The loss weights, as defined in Sec. IV-C, are set to  $\lambda_m = 1.0$ ,  $\lambda_{var} = 0.1$ ,  $\lambda_{vio} = 0.1$ ,  $\lambda_Q = 0.1$ ,  $\lambda_T = 100.0$ ,  $\lambda_X = 10.0$ ,  $\lambda_S = 10.0$ ,  $\lambda_B = 1.0$  and  $\lambda_\xi = 1.0$ .

### A. Evaluation of Scene Flow Performance

We compare the proposed method with the aforementioned approaches using standard evaluation metrics as defined in [36]: end point error (EPE) and 4D average angular error (AAE) error. Each metric is calculated as averages over the entire image and is reported in cm and degrees, respectively. Because it is impossible to calculate the scene flow for an object that is only present in one of the two frames, we also report masked EPE and masked AAE which calculates the desired metrics only on objects that are in both frames. The results are presented in Fig. 6.

All our proposed models outperform the aforementioned approaches both in mean and standard deviation. Furthermore, **OurC** and its variants perform better than the simple model version **OurS** without the correlation layer. This comes at the expense of a higher processing time. However, the most complex model **OurC+vL+Rig** can still run at 8.3 frames per second.

Method	EPE in cm		AAE in degrees		Runtime seconds
	all	masked	all	masked	
PD-Flow[19]	2.830 $\pm$ 4.23	8.041 $\pm$ 5.10	1.607 $\pm$ 2.38	4.572 $\pm$ 2.87	<b>0.046</b>
SR-Flow [28]	2.040 $\pm$ 3.77	6.859 $\pm$ 4.69	1.155 $\pm$ 2.12	3.898 $\pm$ 2.63	$\geq 1$
Jaimez et al. [20]	2.330 $\pm$ 3.94	6.431 $\pm$ 5.20	1.317 $\pm$ 2.20	3.643 $\pm$ 2.91	0.083
OurS	1.643 $\pm$ 3.07	5.324 $\pm$ 3.56	0.928 $\pm$ 1.72	3.020 $\pm$ 2.00	0.059
OurC	1.330 $\pm$ 2.60	4.333 $\pm$ 2.92	0.750 $\pm$ 1.45	2.457 $\pm$ 1.64	0.078
OurC+vL	1.315 $\pm$ 2.57	4.333 $\pm$ 2.95	0.742 $\pm$ 1.44	2.457 $\pm$ 1.66	0.078
OurC + vL + Rig	<b>1.303</b> $\pm$ 2.55	<b>4.290</b> $\pm$ 2.93	<b>0.734</b> $\pm$ 1.43	<b>2.432</b> $\pm$ 1.64	0.121

Fig. 6. Performance of scene flow prediction measured in endpoint error (EPE) and average angular error (AAE) with standard deviation. *Masked* only contains data from objects that appear in both frames. The learned models outperform the baselines in terms of mean error and std **OurC** and its variants perform better than the simple model version **OurS** without the correlation layer.

Method	Precision		Recall		F-measure		Extracted Objects	
	Test	TestSeq	Test	TestSeq	Test	TestSeq	Test	TestSeq
HOMC[22]	<b>0.833</b>	<b>0.797</b>	0.195	0.282	0.111	0.186	3909/64556	1172/11782
OurS	0.697	0.714	0.735	0.749	0.671	0.683	36369/64556	7077/11782
OurC	0.756	0.763	0.757	0.771	0.696	0.711	41274/64556	7839/11782
OurC+vL	0.766	0.768	<b>0.787</b>	<b>0.783</b>	<b>0.730</b>	<b>0.725</b>	<b>43719/64556</b>	<b>8015/11782</b>

Fig. 7. Performance of motion-based segmentation. **Test** refers to the dataset containing repetitions of 2 image frames. **TestSeq** refers to the dataset containing 8 image frames. The proposed models significantly outperform HOMC that requires longer image sequences but cannot rely on the strong depth cue. The performance increase of **OurC+vL** over the simpler models highlights the importance of the correlation layer and the variance and violation loss.

### B. Evaluation of Motion-based Segmentation

We evaluate our model’s ability to perform motion-based segmentation by comparing to HOMC, the state-of-the-art technique by Keuper [22]. This method requires a sequence of RGB images. To satisfy the input requirement of HOMC, we generate an additional test dataset called **TestSeq** following the procedure outlined in Sec. V. In **TestSeq** there are 1302 image sequences each consisting of 8 frames with indices 20, 30, 40, 50, 60, 70, 80 and 90. The original data set only has 2 frames, frame 20 and 80. From this we create the data set **Test** in which these two frames are repeated 5 times (20, 80, 20, 80, 20, 80, 20, 80, 20, 80) such that it can serve as input to HOMC. Keuper [22] provided an executable file upon request. We run HOMC[22] on the sequences with a subsampling of 4 and a prior cut probability of 0.5. For our proposed models, frames 20 and 80 compose the input image pair for all experiments.

To evaluate the segmentation results produced by HOMC and our three network variants, we rely on four metrics that are frequently used in segmentation papers: precision, recall, F-measure, and extracted objects [23]. We compute the metrics on the segmentation of frame 80 by following the convention in [27]. We use an F-measure threshold of 0.75. The results are reported in Fig. 7.

On both datasets, HOMC [22] achieves high precision and low recall values indicating undersegmentation. In **TestSeq**, HOMC extracts more objects with higher recall and F-measure scores than **Test**, emphasizing the dependence on an actual image sequence. All our proposed methods show a significant improvement on the recall, F-measure, and extracted objects metrics while retaining a high precision score. While HOMC relies on a longer sequence of images and takes more than 30 seconds to process the sequence, it does not require depth information. A few example results

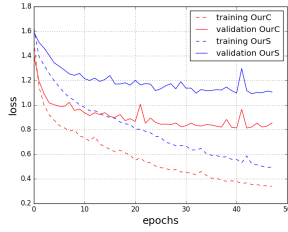


Fig. 8. Loss curve at each epoch during training and validation for our model with and without the correlation layer: **OurC** and **OurS**

are displayed in Fig. 9. These results highlight another advantage of our approach, that the resulting segmentation is dense.

### C. Architecture Design Analysis

1) *Effects of correlation layer:* We report the training and validation loss curve in Fig. 8. **OurC** has a much lower training and validation loss than **OurS**. We also showed that **OurC** outperforms **OurS** both in scene flow prediction and motion-based segmentation. This demonstrates the impact of adding a correlation layer in **OurC**. It forces our model to learn the similarity between consecutive RGB features which makes **OurC** more robust to changes such as lighting conditions or viewpoints.

2) *Effects of using variance and violation loss:* We utilize the variance loss to reduce the statistical variance of predicted trajectory features. The violation loss penalizes outliers in the training process. Compared to **OurC**, **OurC+vL** improves motion-based segmentation, but only leads to small improvements on scene flow prediction.

3) *Effects of using rigid motion cues:* The best scene flow prediction performance is achieved by adding rigid constraints (**OurC+vL+Rig**). However the improvement over **OurC** is only marginal. The difference to **OurS** remains significant, underlining the importance of correlation layer.

### D. Results and Analysis on Real World Data

Finally, we demonstrate the networks ability to perform in a real world setting. We recorded real RGB-D data with the Intel RealSense SR300 Camera. The data includes large displacements, occlusions, and collisions. It was captured using a diverse set of objects with varying geometries, textures, and colors. Note that we do not have any ground truth annotations and that the model is not fine-tuned to transfer from synthetic to real data.

We apply HOMC [22] on the stream of real data as one long sequence. We use our **OurC+vL+Rig** model to process real data sequences. Every pair of consecutive images forms one image pair which are fed into our neural network. Some example images and corresponding outputs are displayed in Fig. 10. The accurate real world segmentation and scene flow prediction results strongly indicate the small sim-to-real transfer gap of the proposed model.

There are still some failure cases including inaccurate object boundaries due to noisy sensor data and false positive segmentations due to varied lighting conditions. Also if two objects are moving along extremely similar trajectories, it is difficult to segment them. This could be potentially alleviated by concatenating rotational motion to the trajectory

feature. Other limitations of our method include: inability to generalize to non-flat surfaces or non-rigid objects. The generalization problem of learning-based methods could be mitigated by transfer-learning techniques e.g. [9].

## VII. CONCLUSION

We proposed a deep neural network architecture that given two consecutive RGB-D images can accurately estimate object scene flow and motion-based object segmentation. We demonstrated this on a new and challenging, synthetic data set that contains a large variety of graspable objects moving simultaneously. We showed that the correlation layer makes a crucial difference to training time and accuracy and outperforms state of the art baselines in scene flow prediction and motion-based segmentation. Additionally, we showed how our approach performs on real RGB-D data when only trained on synthetic data. The results look qualitatively more accurate than baseline methods. Overall, we demonstrated the power of learning based methods over traditional methods in situations of large displacements and strong occlusions. In future work, we will explore how this approach enables agile, robotic manipulation in cluttered scenes.

## REFERENCES

- [1] J. Bohg, K. Hausman, B. Sankaran, O. Brock, D. Kragic, S. Schaal, and G. S. Sukhatme. Interactive perception: Leveraging action in perception and perception in action. *IEEE Transactions on Robotics*, 2017.
- [2] W. Brendel and S. Todorovic. Video object segmentation by tracking regions. In *Computer Vision, 2009 IEEE 12th Int. Conf. on*, 2009.
- [3] T. Brox and J. Malik. Object segmentation by long term analysis of point trajectories. *Computer Vision—ECCV 2010*, 2010.
- [4] D. J. Butler, J. Wulff, G. B. Stanley, and M. J. Black. A naturalistic open source movie for optical flow evaluation. In *European Conf. on Computer Vision*. Springer, 2012.
- [5] Angel X. Chang, Thomas Funkhouser, Leonidas Guibas, Pat Hanrahan, Qixing Huang, Zimo Li, Silvio Savarese, Manolis Savva, Shuran Song, Hao Su, Jianxiong Xiao, Li Yi, and Fisher Yu. ShapeNet: An Information-Rich 3D Model Repository. Technical Report arXiv:1512.03012 [cs.GR], Stanford University — Princeton University — Toyota Technological Institute at Chicago, 2015.
- [6] A. M. Cheriyyadat and R. J. Radke. Non-negative matrix factorization of partial track data for motion segmentation. In *Computer Vision, 2009 IEEE 12th Int. Conf. on*. IEEE, 2009.
- [7] E. Coumans. Bullet physics simulation. In *ACM SIGGRAPH 2015 Courses*, SIGGRAPH '15. ACM, 2015.
- [8] A. Dosovitskiy, P. Fischery, E. Ilg, P. Häusser, C. Hazirbaş, V. Golkov, P. van der Smagt, D. Cremers, and T. Brox. FlowNet: Learning optical flow with convolutional networks. In *2015 IEEE Int. Conf. on Computer Vision (ICCV)*, 2015.
- [9] Yaroslav Ganin and Victor Lempitsky. Unsupervised domain adaptation by backpropagation. In *International Conference on Machine Learning*, pages 1180–1189, 2015.
- [10] A. Geiger, P. Lenz, C. Stiller, and R. Urtasun. Vision meets robotics: The kitti dataset. *Int. Journal of Robotics Research (IJRR)*, 2013.
- [11] V. Golyanik, K. Kim, R. Maier, M. Nießner, D. Stricker, and J. Kautz. Multiframe scene flow with piecewise rigid motion. In *Proceedings of the Int. Conf. on 3D Vision (3DV)*, 2017.
- [12] J. Gottfried, J. Fehr, and C. Garbe. Computing range flow from multi-modal kinect data. In *Int. Symposium on Visual Computing*, 2011.
- [13] M. Grundmann, V. Kwatra, M. Han, and I. Essa. Efficient hierarchical graph-based video segmentation. In *Computer Vision and Pattern Recognition (CVPR), 2010 IEEE Conf. on*. IEEE, 2010.
- [14] M. Gschwandtner, R. Kwitt, A. Uhl, and W. Pree. Blender: blender sensor simulation toolbox. *Advances in Visual Computing*, 2011.
- [15] S. Hadfield and R. Bowden. Scene flow estimation using intelligent cost functions. In *British Conf. on Machine Vision*, 2014.
- [16] K. He, X. Zhang, S. Ren, and J. Sun. Deep residual learning for image recognition. In *Proceedings of the IEEE conference on computer vision and pattern recognition*, 2016.

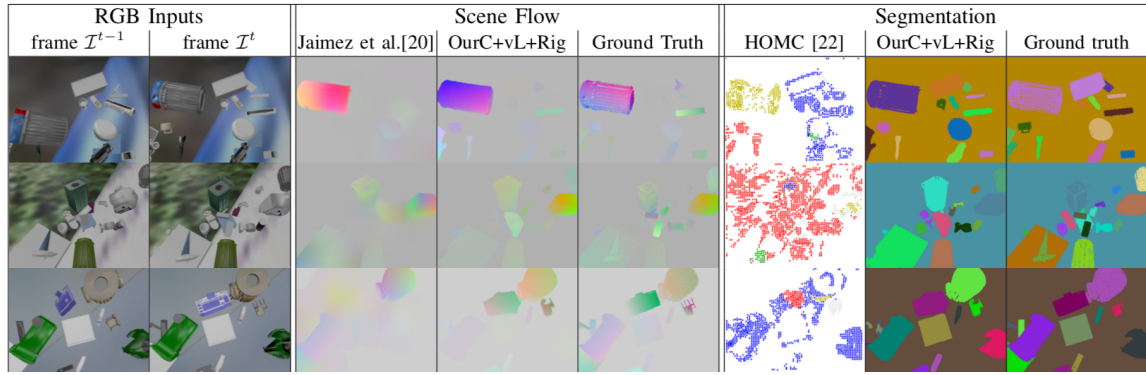


Fig. 9. Performance comparison of the proposed method on our synthetic data set. First two columns show RGB inputs, next columns are Scene Flow from Jaimez et al. [20], our method, and the ground truth, the final three columns correspond to segmentation results from HOMC [22], our method, and the ground truth. In scene flow images, green, blue, red intensities are proportional to the velocities along  $X$ ,  $Y$ ,  $Z$  respectively. In the HOMC segmentation, colored pixels (not gray or white) have been successfully clustered with longer trajectories to produce valid segmentations.

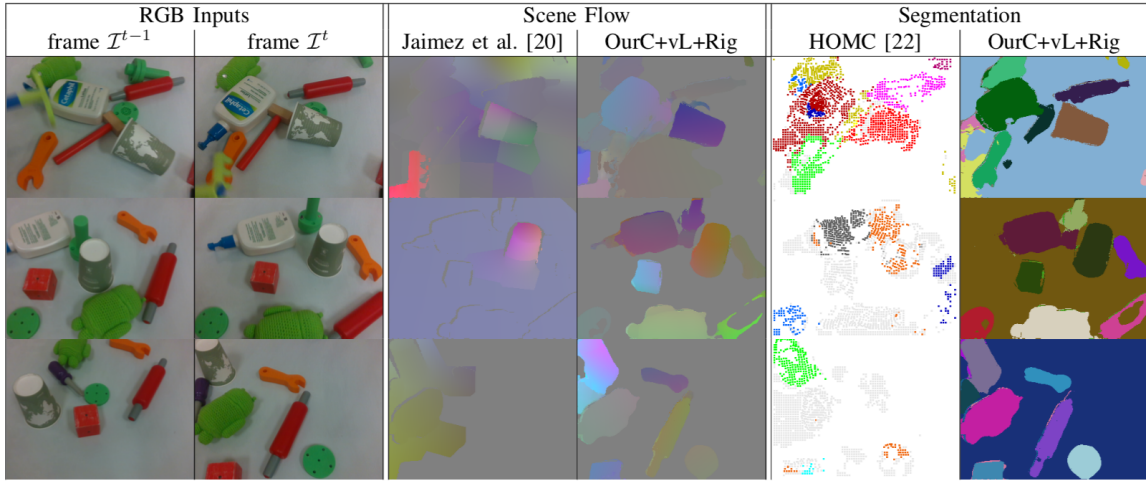


Fig. 10. Performance comparison of the proposed method on the real-world data set. First two columns show RGB inputs, next columns are Scene Flow from Jaimez et al. [20] and our methods, last two columns correspond to segmentation results from HOMC [22] and our method.

- [17] E. Herbst, X. Ren, and D. Fox. Rgb-d flow: Dense 3-d motion estimation using color and depth. In *Robotics and Automation (ICRA), 2013 IEEE Int. Conf. on.* IEEE, 2013.
- [18] E. Ilg, N. Mayer, T. Saikia, M. Keuper, A. Dosovitskiy, and T. Brox. FlowNet 2.0: Evolution of optical flow estimation with deep networks. In *IEEE Conf. on Computer Vision and Pattern Recognition*, 2017.
- [19] M. Jaimez, M. Souiai, J. Gonzalez-Jimenez, and D. Cremers. A primal-dual framework for real-time dense rgb-d scene flow. In *Robotics and Automation (ICRA), 2015 IEEE Int. Conf. on*, 2015.
- [20] M. Jaimez, C. Kerl, J. Gonzalez-Jimenez, and D. Cremers. Fast odometry and scene flow from rgb-d cameras based on geometric clustering. In *2017 IEEE International Conference on Robotics and Automation (ICRA)*, May 2017. doi: 10.1109/ICRA.2017.7989459.
- [21] P. Ji, H. Li, M. Salzmann, and Y. Dai. Robust motion segmentation with unknown correspondences. In *European Conf. on computer vision*. Springer, 2014.
- [22] M. Keuper. Higher-order minimum cost lifted multicuts for motion segmentation. *2017 IEEE Int. Conf. on Computer Vision (ICCV)*, 2017.
- [23] M. Keuper, B. Andres, and T. Brox. Motion trajectory segmentation via minimum cost multicuts. In *IEEE Int. Conf. on Computer Vision (ICCV)*, 2015.
- [24] D. Kingma and J. Ba. Adam: A method for stochastic optimization. In *Int. Conf. on Learning Representations (ICLR)*, 2015.
- [25] N. Mayer, E. Ilg, P. Häusser, P. Fischer, D. Cremers, A. Dosovitskiy, and T. Brox. A large dataset to train convolutional networks for disparity, optical flow, and scene flow estimation. In *Proceedings of the IEEE Conf. on Computer Vision and Pattern Recognition*, 2016.
- [26] M. Menze and A. Geiger. Object scene flow for autonomous vehicles. In *Proceedings of the IEEE Conf. on Computer Vision and Pattern Recognition (CVPR)*, 2015.
- [27] P. Ochs, J. Malik, and T. Brox. Segmentation of moving objects by long term video analysis. *IEEE transactions on pattern analysis and machine intelligence*, 2014.
- [28] J. Quiroga, T. Brox, F. Devernay, and J. Crowley. Dense semi-rigid scene flow estimation from rgbd images. In *European Conference on Computer Vision*, pages 567–582. Springer, 2014.
- [29] H. Rahmati, R. Dragon, O. Aamo, L. Van Gool, and L. Adde. Motion segmentation with weak labeling priors. In *German Conf. on Pattern Recognition*. Springer, 2014.
- [30] S. Ren, K. He, R. Girshick, and J. Sun. Faster r-cnn: Towards real-time object detection with region proposal networks. In *Advances in neural information processing systems*, 2015.
- [31] L. Shao, A. X. Chang, H. Su, M. Savva, and L. Guibas. Cross-modal attribute transfer for rescaling 3D models. In *Proceedings of the Int. Conf. on 3D Vision (3DV)*, 2017.
- [32] K. Simonyan and A. Zisserman. Very deep convolutional networks for large-scale image recognition. *CoRR*, abs/1409.1556, 2014.
- [33] S. Vedula, P. Rander, R. Collins, and T. Kanade. Three-dimensional scene flow. *IEEE transactions on pattern analysis and machine intelligence*, 2005.
- [34] C. Vogel, K. Schindler, and S. Roth. Piecewise rigid scene flow. In *2013 IEEE Int. Conf. on Computer Vision*, 2013.
- [35] J. Xiao, J. Hays, K. A. Ehinger, A. Oliva, and A. Torralba. Sun database: Large-scale scene recognition from abbey to zoo. In *Computer vision and pattern recognition (CVPR), 2010 IEEE Conf. on.* IEEE, 2010.
- [36] Z. Yan and X. Xiang. Scene flow estimation: A survey. *CoRR*, abs/1612.02590, 2016.
- [37] V. Zografos, R. Lenz, R. Ringaby, M. Felsberg, and K. Nordberg. Fast segmentation of sparse 3d point trajectories using group theoretical invariants. In *Asian Conf. on Computer Vision*. Springer, 2014.